

Automated Classification of Whole-Body SPECT Bone Scan Images with VGG-Based Deep Networks

Qiang Lin

School of Mathematics and
Computer Science, Northwest
Minzu University, China
qianglin@xbmu.edu.cn

Zhengxing Man

School of Mathematics and
Computer Science, Northwest
Minzu University, China
jismxy@xbmu.edu.cn

Yongchun Cao

School of Mathematics and
Computer Science, Northwest
Minzu University, China
cych33908@xbmu.edu.cn

Haijun Wang

Department of Nuclear
Medicine, Gansu Provincial
Hospital, China
whjgzl@163.com

Abstract: Single Photon Emission Computed Tomography (SPECT) imaging has the potential to acquire information about areas of concerns in a non-invasive manner. Until now, however, deep learning based classification of SPECT images is still not studied yet. To examine the ability of convolutional neural networks on classifying whole-body SPECT bone scan images, in this work, we propose three different two-class classifiers based on the classical Visual Geometry Group (VGG) model. The proposed classifiers are able to automatically identify that whether or not a SPECT image include lesions via classifying this image into categories. Specifically, a pre-processing method is proposed to convert each SPECT file into an image via balancing difference of the detected uptake between SPECT files, normalizing elements of each file into an interval, and splitting an image into batches. Second, different strategies were introduced into the classical VGG16 model to develop classifiers by minimizing the number of parameters as many as possible. Lastly, a group of clinical whole-body SPECT bone scan files were utilized to evaluate the developed classifiers. Experiment results show that our classifiers are workable for automated classification of SPECT images, obtaining the best values of 0.838, 0.929, 0.966, 0.908 and 0.875 for accuracy, precision, recall, F-1 score and AUC value, respectively.

Keywords: Image classification, nuclear medicine, SPECT imaging, deep learning, VGG 16.

Received November 1, 2020; accepted January 19, 2022

<https://doi.org/10.34028/iajit/20/1/1>

1. Introduction

The past few decades have witnessed a significant rise in demand for medical image analysis because medical imaging provides an important base to display and differentiate the pathological tissue from the normal field of the body. Specifically, the structural imaging acquires anatomic/morphological structures of organs and tissues while the physiological/functional imaging captures functional changes in pathological tissues of the body. Due to the superior capability of Convolutional Neural Network (CNN) on automatically extracting from the low-level to high-level features from images [8], a large number of CNN-based work has been done on the structural image (i.e., Computed Tomography (CT) and Magnetic Resonance Imaging (MRI) analysis including image segmentation and classification [7, 9, 17, 18, 20].

The commonly used functional imaging techniques include MR lymphography, perfusion CT, diffusion-weighted imaging, MR spectroscopy, dynamic contrast-enhanced MRI, blood oxygenation level-dependent MRI, Single Photon Emission Computed Tomography (SPECT), and Positron Emission Tomography (PET) [2]. As a most well-established functional imaging modality, SPECT has been widely used since the early 1990s and over 18 million SPECT scans are conducted each year in the

United States.

SPECT imaging works by injecting radionuclides into a patient's body and capturing information about areas of concerns, e.g., lesions and organs [4]. Imaging equipment picks up the emitted gamma rays to produce a map of the inside of a body and identify the body areas. The data acquired by SPECT imaging is stored in a file that is, in essence, a matrix. The elements in this matrix are the detected counts of uptake, which differs from the natural images in which the pixel value ranges from 0 to 255. The resolution of a SPECT image is relatively low. A whole-body SPECT image, for example, has a size of 256 (width)×1024 (height).

Compared to the structural and other functional imaging modalities, it is more difficult for SPECT to develop a comparable and high-performance classifier for the purpose of automated classification of diseases [2]. Using CNN, classifying SPECT bone scan images for diagnosing disease is still in its infancy. Currently, only few work has been done to classify partial- instead of whole-body SPECT images, targeting at automated detection or diagnosis of neurodegenerative disorder [6,12,13,15], thyroid disease [10,11], and coronary artery disease [20]. The CNN models used mainly include LeNet [3], AlexNet [1], DenseNet [5] and VGGNet [19]. An open dataset PPMI (<https://www.ppmi-info.org/>) was frequently used in

existing works [12, 13, 15].

To examine the ability of CNN-based techniques on classifying whole-body SPECT bone scan images, in this work, we propose three two-class classifiers based on the classical Visual Geometry Group (VGG) model. The proposed classifiers can identify that whether one or more metastatic lesions present in a whole-body SPECT image. Specifically, we first propose a pre-processing method to convert each SPECT file into an image through balancing difference of the detected counts of uptake between SPECT files, normalizing elements of each file into an interval, and splitting an image into one or more batches. Second, various strategies were adopted to construct classifiers by minimizing the number of parameters of VGG 16 as many as possible. Lastly, a group of clinical whole-body SPECT bone scans were used to evaluate the proposed classifiers. Experiment results show that our classifiers are workable for the two-class classification task, with obtaining the best values of 0.838, 0.929, 0.966, 0.908, and 0.875 for accuracy, precision, recall, F-1 score and AUC value, respectively.

The rest of this paper is organized as follows. We provide in section 2 the materials and methods used in this work. We report in section 3 the experimental results. In section 4, we conclude this work and point out the future research directions.

2. Materials and Methods

In this section, the used whole-body SPECT bone scan images, the pre-processing method conducted on image data, and the proposed classifiers based on VGG model will be detailed.

2.1. Dataset and Pre-Processing

2.1.1. SPECT Imaging Data

SPECT is a typical non-invasive imaging technique, which captures uptake of radiopharmaceutical by using imaging device outside the body of a patient. Currently, SPECT imaging is widely used for clinical examination of various diseases including tumors, bone metastasis, arthritis, and neurodegenerative disorders.

A SPECT examination generates two Digital Imaging and Communications in Medicine (DICOM) files (.dcm), recording the anterior- and posterior-view image of the body, respectively. Each DICOM file is a matrix of the detected uptake represented by a 16-bit unsigned integer. As mentioned previously, the size of the matrix is 256×1024 , enabling to show most of the body of the patient.

The data of SPECT imaging files used in this work were acquired during diagnosing various physiological diseases using an equipment Siemens SPECT ECAM in Gansu Provincial Hospital from Jan 2016 to Nov 2018. The emitted gamma rays from radiopharmaceutical $^{99m}\text{Tc-MDP}$ that was intravenously injected into the

body of a patient in advance were collected by the imaging equipment to produce a map of the inside of a body and identify the body areas, e.g., lesions and organs.

Figure 1 depicts the visual presentation of a SPECT file captured from the anterior of the body in the form of RGB image. Three lesions are present in the images, which have been diagnosed as degenerative change in the spine and arthritis in both the left and right knees by physicians. Drug residue in the urinary bladder has also been detected as high-uptake area in the SPECT images, which often challenges CNN-based image analysis due to its similar visual characteristics with lesions.

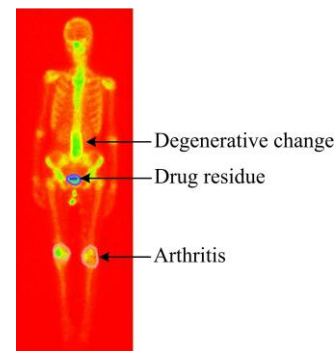


Figure 1. A visual presentation of an anterior SPECT file.

The SPECT files differ from the natural images and structural medical images by the wide range of uptake, making the traditional machine learning algorithms that use handcrafted features unsuitable for distinguishing diseased images from the rest. As an example, Table 1 provides the statistical analysis of the detected uptake of SPECT files collected in 2017 and 2018. The sources of the variance vary, relying on the radiopharmaceutical injected, waiting period after patients were injected with a radioactive substance, and imaging device.

Table 1. The detected counts of uptake in the selected SPECT bone scan files in our datasets acquired in 2017 and 2018.

	Min	80%	90%	Max	Mode
17-Anterior	4	187	378	9805	31
17-Posterior	4	144	333	11070	31
18-Anterior	4	243	363	12668	34
18-Posterior	4	186	360	15738	34

We call the SPECT files (i.e., both the anterior and posterior) collected from each examination as a medical case. There are finally 3831 medical cases in our dataset after removing those files with uncertain morphology, contamination, and interference. The diseases included in the dataset are bone metastasis, inflammation, and degenerative changes. We chose 3271 SPECT files after converting them into images for training the proposed classifiers and the rest 560 cases for testing. In our two-class classification problem, a SPECT file that includes at least one lesion is regarded as positive (i.e., diseased); otherwise, it is a negative image. The rate of the positive and negative files is about 3.3: 1 in both the training and test subsets.

2.1.2. Converting SPECT File to Image

As mentioned previously, a SPECT file is a data matrix of the detected uptake. The CNN models like VGG and Inception cannot work directly on a data matrix if the transfer learning technique is used. We therefore need to convert every SPECT file to an image in the form of that the deep models require. Formally, we use matrix rd to represent a DICOM file as follows.

$$rd = \begin{bmatrix} rd_{11} & rd_{12} & \cdots & rd_{1m} \\ rd_{21} & rd_{22} & \cdots & rd_{2m} \\ \vdots & \vdots & \ddots & \vdots \\ rd_{n1} & rd_{n2} & \cdots & rd_{nm} \end{bmatrix} \quad (1)$$

where rd_{ij} ($1 \leq i \leq m$, $1 \leq j \leq n$) denotes the detected uptake with a 16-bit unsigned integer and $m=256$, $n=1024$ for a whole-body SPECT bone scan file.

The first task is to alleviate the difference of the detected uptake between medical cases. Let M denote the mode as provided in Table 1, an element rd_{ij} in rd can be squeezed according to Equation (2).

$$rd_{ij} = \begin{cases} rd_{ij}(1-\alpha), & \text{if } rd_{ij} \geq m \cdot M \\ rd_{ij}, & \text{Otherwise} \end{cases} \quad (2)$$

where α is a random number between $[0, 0.05]$ and m is a constant. A value of 10 for m performs well in the experiment.

The second task is to normalize each element of the matrix into an interval $[a, b]$ by calculating a coefficient factor k according to Equation (3).

$$k = \frac{b-a}{rd_{Max} - rd_{Min}} \quad (3)$$

where rd_{Max} and rd_{Min} is the maximum and minimum of elements in the squeezed rd , respectively.

The normalized matrix is treated as an image, in which each element ranges from a to b . In the proposed classifiers, a and b will be set as 0 and 1, respectively.

The last task is to split a 256×1024 SPECT image into patches. To do so, two schemes are used as follows.

- A positive SPECT image will be conditionally split into one or more patches. In this case, we ensure that each of the split patch contains at least one lesion and there is no overlap between any two adjacent patches.
- A negative SPECT image will be deterministically split into four patches at equal intervals. In this case, we ensure that the four patches cover all non-empty regions of this image together.

Figure 2 depicts the process of splitting patches from a negative image (left panel) and a positive image (right panel). Specifically, the negative image is split into four patches and the positive one is split into two patches. The first patch in the positive image contains an arthritic lesion ‘a1’ and two metastatic lesions ‘bm1’ and ‘bm2’.

The second patch contains two metastatic lesions ‘bm3’ and ‘bm4’.

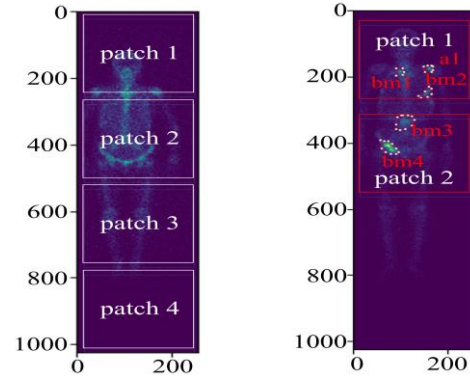


Figure 2. An example of splitting SPECT images into patches.

How to determine that a SPECT image is positive or not is implemented by physicians labeling this image. We developed an annotation system based on LabelMe (<http://labelme.csail.mit.edu/Release3.0/>) released by MIT with a Web interface for labelling SPECT images. As depicted in Figure 3, each labelled area in an image will be annotated with a self-defined symbol combined with the name of disease or body part. The annotation results for all images serve as ground truth in experiments and will be organized in an annotation file, which will be fed into the classifiers.



Figure 3. LabelMe-based SPECT image annotation system.

Specifically, three human experts consisting of one nuclear medicine physician, one nuclear medicine nurse and one trained computer vision expert manually label every image independently. An image will be annotated as a positive image if the majority of the human experts regard this image contain one or more hotspots.

Using the operations above, 8701 patches of 224×224 were finally extracted from 3271 whole-body bone scan images for training the classifiers and 1490 patches from 560 images for testing the classifiers (see Table 2).

Table 2. The used dataset in this paper.

	Training data		Test data	
	Patches	Images	Patches	Images
Positive	4821	2301	830	395
Negative	3880	970	660	165

2.2. VGG-Based Classifiers

Several classical CNN models were adopted to develop automated classifiers based on the Tensor flow platform for classification of SPECT images, including Xception, VGG16, VGG19, ResNet, Inception-v3, and ResNet-v2. However, the accuracy obtained by Xception, ResNet, Inception-v3, and ResNet-v2 is less than 60% and VGG16 performs better than VGG19 on classifying SPECT images. We therefore chose VGG16 as a base model to develop our classifiers for classifying SPECT images.

Figure 4 shows the network structure of VGG16. The number of parameter in each convolution is displayed and the total number of parameters is 138357544.

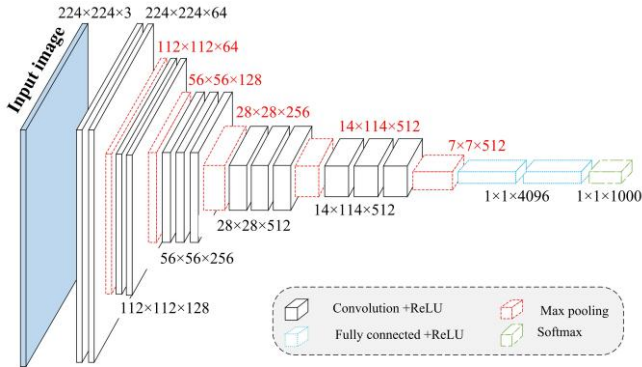


Figure 4. The network structure of the classical VGG16 model.

For a given input image $I_{x,y}$, the k -th layer output of this image after a convolution operation that the l -th convolutional kernel is defined in Equation (4).

$$C = I_{x,y} \times K, \quad (4)$$

where K is the l -th convolutional kernel of the k -th layer, and x, y are spatial localities.

A rectified linear unit (ReLU) function makes the elements with a value < 0 become 0, which is defined in Equation (5) [14].

$$\text{ReLU}(x) = \max(0, x), \quad (5)$$

where x is a pixel value in an image.

A Softmax function is defined as follows.

$$f(x_j) = \frac{e^{x_j}}{\sum_{i=1}^n e^{x_i}}, \quad (6)$$

where $f(x_j)$ is the score of the j -th output node, x_j is the net input to the j -th output node, and n is the number of output nodes. In fact, all of the output values $f(x)$ are a probability, which is between 0 and 1, and their sum is 1 [17].

Based on the classical model VGG 16, in this work,

we propose three different classifiers by minimizing the parameters of VGG16, which are illustrated in Figure 5.

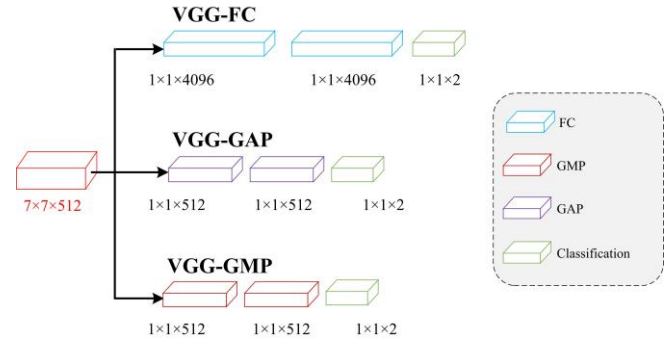


Figure 5. The proposed classifiers VGG-FC, VGG-GAP, and VGG-GMP based on the classical VGG16 model.

2.2.1. VGG-FC Classifier

Since the two fully connected layers (i.e., FC1 and FC2) have too many parameters, the classical VGG16 model would be prone to overfitting if a relatively smaller dataset is applied. For our classifier VGG-FC (VGG16 with fully connected layer) that uses transfer learning technique, we remain all parameters unchanged before the prediction layer and replace only the prediction layer with classification layer. As a result, there are overall 134268738 parameters for our classification problem and only 8914 ($4096 \times 2 + 2$) parameters need to be trained in the proposed VGG-FC classifier.

2.2.2. VGG-GAP Classifier

We use Global Average Pooling (GAP) layer instead of the fully connected layers in the classification model to minimize the number of parameters when the transfer learning is used for training the deep model. So, only 14714688 parameters need to be trained in our classifier VGG-GAP. The reason is that the GAP layer has no parameter and its output is a 512D vector. For our two-class classification problem, the number of parameters that need to be trained is 1026 ($512 \times 2 + 2$) if we remain the features extracted by convolutional layer unchanged.

2.2.3. VGG-GMP Classifier

We use GMP instead of GAP in the classification model to further minimize the number of parameters when the transfer learning is used for training the model. So, only 14714688 parameters need to be trained in our classifier VGG-GMP. Similar to VGG-GAP, the GMP layer has no parameter and its output is a 512D vector. For our two-class classification problem, the number of parameters that need to be trained is 1026 ($512 \times 2 + 2$) if we remain the features extracted by convolutional layer unchanged.

3. Experimental Evaluation

We present an experimental evaluation in this section

conducted on the clinical whole-body SPECT bone scan images as shown in Table 2.

3.1. Experimental Setup

All experimental data of SPECT images in Table 2 were stored in a MongoDB database for access by the VGG-based classifiers. The annotation process produces data that follow the Tensorflow Dataset form.

For our two-class classification problem, a SPECT image will be categorized into one of the following four categories.

- True Positive (TP): a diseased SPECT image will be correctly identified as positive image;
- True Negative (TN): a normal SPECT image will be correctly identified as negative image;
- False Positive (FP): a normal SPECT image will be incorrectly identified as positive image;
- False Negative (FN): a diseased SPECT image will be incorrectly identified as negative image.

Based on the categories mentioned above, we now define the evaluation metrics (see Table 3).

It is desired that a good classifier can obtain high True Positive Rate (TPR) and low False Positive Rate (FPR) simultaneously. By regarding TPR as x -axis and FPR as y -axis, the area under the curve is defined as

Table 3. The used evaluation metrics in this paper.

Metric	FPR	TNR	NPV	FDR	FNR	TPR
Definition	$FP/(FP+TN)$	$TN/(TN+FP)$	$TN/(TN+FN)$	$FP/(TP+FP)$	$FN/(TN+FP)$	$TP/(TP+FN)$
Metric	Accuracy		Precision	Recall	F-1 score	
Definition	$(TP+TN)/(TP+FP+TN+FN)$		$TP/(TP+FP)$	$TP/(TP+FN)$	$2(Precision \times Recall)/(Precision + Recall)$	

Table 4. The values of different evaluation metrics obtained by three different classifiers.

Metric	FPR	TNR	NPV	FDR	FNR	TPR	Accuracy	Precision	Recall	F-1 Score
VGG-FC	0.368	0.632	0.500	0.080	0.129	0.871	0.830	0.920	0.830	0.895
VGG-GAP	0.305	0.695	0.437	0.071	0.183	0.817	0.796	0.929	0.817	0.870
VGG-GMP	0.789	0.211	0.556	0.143	0.034	0.966	0.838	0.857	0.966	0.908

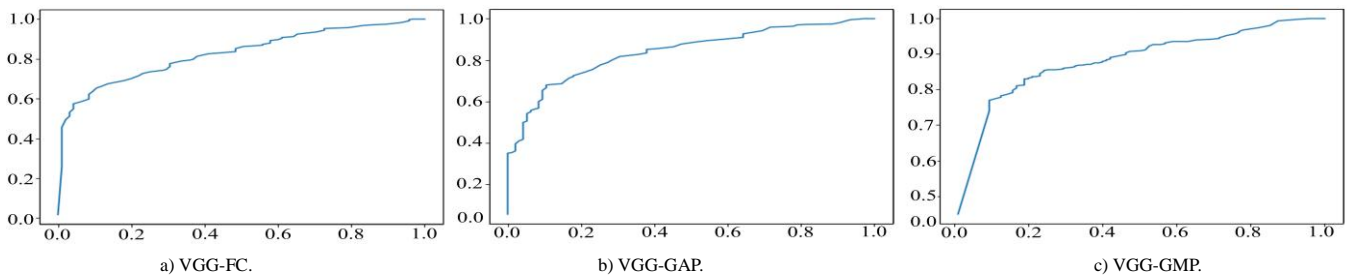


Figure 7. The ROC curves obtained by the tree different deep classifiers.

Figure 7 depicts the ROC curves of the three classifiers on classifying whole-body SPECT bone scan images.

The corresponding AUC values are provided in Table 5.

The proposed VGG-based classifiers are workable for classifying SPECT bone scan images. The high AUC values in Table 5 further show that VGG-GMP performs better than the rest classifiers. We can conclude that the deep learning technique has the potential to be used as a kind of emerging techniques for

AUC value. The more the AUC value, the high performance of the classifier obtains.

3.2. Experimental Results

For the test dataset consisting of 560 SPECT images as shown in Table 2, Figure 6 reports the confusion matrices obtained by three different classifiers.

		The predicted						The predicted			
Ground truth		P	N	Ground truth		P	N	Ground truth		P	N
	P	405	60		P	380	85		P	449	16
N	35	60	N	29	66	N	75	20			

Figure 6. Confusion matrices of the built classifiers with P =Positive and N =Negative. (Left: VGG-GMP; Middle: VGG-GAP; Right: VGG-FC).

Table 4 reports the values of evaluation metrics obtained by three classifiers. It can be seen that VGG-GMP performs better than the others with respect to the defined evaluation metrics. Specifically, VGG-GMP is more suitable for identifying the positive samples of SPECT images with a value of 0.966 for *Recall* metric. However, all classifiers underperform on classifying the negative SPECT images.

automated diagnosis of disease with the SPECT images.

Table 5. The AUC values of three different classifiers.

AUC	Upper	Lower	Average
VGG-FC	0.8313	0.8206	0.8259
VGG-GAP	0.8445	0.8363	0.8404
VGG-GMP	0.8891	0.8617	0.8754

4. Discussion

We provide in this section a brief discussion about the reasons that cause misclassification of SPECT images.

- Model aspect: convolutional neural network has been widely applied in various fields such as intelligent transportation system [16]. However, the classical VGG 16 has too many parameters, which makes VGG-FC inefficient on classifying SPECT images. On the contrary, only 1026 parameters need to be trained for VGG-GAP and VGG-GMP. Overfitting can be avoided because no parameter needs to be optimized in the global average pooling of VGG-GAP and global maximum pooling of VGG-GMP. Furthermore, the global pooling layer is more robust to spatial translations of the input than the fully connected layer by summing out the spatial information of images. A global pooling operation has the potential to generate one feature map for each corresponding category of the SPECT image classification task since it is more native to the convolution structure in CNN models. The feature maps extracted by VGG-GAP/GMP are therefore easily interpreted as the categories confidence maps. Moreover, global maximum pooling is more suitable for extracting information of lesions in SPECT images by alleviating deviation of estimated mean value caused by parameter error in convolution layer. In image classification task, global maximum pooling has the potential to select those distinguishable features from images. Despite the tremendous success in a variety of various applications, CNN is far from perfect at present [21]. For SPECT image analysis, a CNN does not exploit the diagnostic features that have been proved more discriminative. Existing CNN-based research efforts focus mainly on supervised learning; however, available large and labelled SPECT datasets are far from abundant for training supervised CNN learning models.
- Data aspect: it can be seen from Tables 4 and 5 that VGG-based SPECT image classification is still in its infancy. The limited datasets of labelled SPECT images (e.g., 3271 images for training and 560 images for test in our dataset) greatly challenge such a field. It is often difficult to develop a large dataset that contains various diseases acquired from different patient cohorts due to the rarity of diseases and patient privacy. Furthermore, it is subjective, time-consuming, and labor-intensive to manually annotate and label low-resolution whole-body scintigraphic images. Although the transfer learning can be used to alleviate the problem of the lack of sufficient images to some extent, how to fine-tune the parameters from natural images to SPECT images is still an open problem. Imbalanced data refers to a scenario in which the number of instances of one category is scanty in comparison to other classes. Such a problem presents in our dataset of SPECT images, where the rate of positive and negative samples is about 3.3:1 for training dataset. This would cause our classifiers to be more sensitive

to detecting the diseased images and less sensitive to the normal ones. The VGG-GMP classifier achieves a value of 0.211 and 0.556 for *TNR* and *NPV*, respectively. The imbalance problem is also present in the subcategories of those diseased SPECT images, resulting in a skewed classification accuracy.

- SPECT imaging aspect: in comparison with the structural imaging techniques like CT and MRI, SPECT is often accompanied by misregistration, respiration, truncation, and highly attenuating foreign bodies. All these artifacts and pitfalls challenge image analysis to some extent. During SPECT bone scanning that can take 2 hours or more, a patient may fall asleep while a system acquires the position of a bed. When the bed shifts to the next scanning position, the patient is often startled. As such, a SPECT image may be marred by motion artifacts. It is also difficult to distinguish tumor progression from a flare response if a bone scan is performed right after a treatment. In addition, if a patient who has undergone recent surgery such as knee replacements, SPECT bone imaging would produce false-positive results. What is more important is that how to reliably recognize normal variants as they can mimic pathology since the pattern of tracer uptake in the sternum, head, and neck region is often variable.

5. Conclusions

Focusing on the automated classification of whole-body SPECT images, in this work, we have proposed three VGG-based classifiers. First, the pre-processing process of converting an original DICOM file to the image form required by VGG model was proposed. Second, various strategies were introduced to the classical VGG16 to construct different classifiers by minimizing the number of parameters as many as possible. Lastly, a group of clinical whole-body SPECT bone scan images were used to evaluate the proposed classifiers. Experiment results have shown that our classifiers are workable for automated classification of SPECT images, obtaining the best values of 0.838, 0.929, 0.966, 0.908 and 0.8754 for accuracy, precision, recall, F-1 score and AUC value, respectively.

We plan to extend this work in the following three directions in the future. First, we intend to collect more data of SPECT imaging with various disease categories and fine-tune the developed classifiers so that they work in real computer-aided diagnosis systems for improving physicians' diagnosis efficiency. Second, we attempt to develop CNNs-based multiclass classification networks with large datasets for reliable disease diagnosis. Lastly, we plan to exploit the nature of the extracted features before a classification process and incorporate the diagnostic features into a CNN-based classifier to achieve higher classification performance.

Acknowledgments

This work was supported by the Youth Ph.D. Foundation of Education Department of Gansu Province (2021QB-063), Natural Science Foundation of Gansu Province (20JR5RA511), Fundamental Research Funds for the Central Universities (31920210013, 31920220020, 31920220054), Key R&D Plan of Gansu Province (21YF5GA063), Gansu Provincial First-class Discipline Program of Northwest Minzu University (11080305), and Program for Innovative Research Team of SEAC ([2018] 98).

Conflicts of Interest

The authors declare no conflict of interest.

References

- [1] Chen B., Deng W., and Du J., “Noisy Softmax: Improving the Generalization Ability of DCNN via Postponing the Early Softmax Saturation,” in *Proceedings of IEEE Conference on Computer Vision and Pattern Recognition*, Honolulu, pp. 4021-4030, 2017.
- [2] Figueiras R., Goh V., Padhani A., Naveira A., Caamaño A., and Martin C., “The Role of Functional Imaging in Colorectal Cancer,” *American Journal of Roentgenology*, vol. 195, no. 1, pp. 54-66, 2010.
- [3] Fukushima K., “Neocognitron: A Hierarchical Neural Network Capable of Visual Pattern Recognition,” *Neural Networks*, vol. 1, no. 2, pp. 119-130, 1988.
- [4] Haidekker M., *Nuclear Imaging Medical Imaging Technology*, Springer, 2013.
- [5] Huang G., Liu Z., Maaten LVD., and Weinberger K., “Densely Connected Convolutional Networks,” in *Proceedings of IEEE Conference on Computer Vision and Pattern Recognition*, Honolulu, pp. 2261-2269, 2017.
- [6] Iizuka T., Fukasawa M., and Kameyama M., “Deep-Learning-Based Imaging Classification Identified Cingulate Island Sign in Dementia with Lewy Bodies,” *Scientific Reports*, vol. 9, no. 1, pp. 8944, 2019.
- [7] Ker J., Wang L., Rao J., and Lim T., “Deep Learning Applications in Medical Image Analysis,” *IEEE Access*, vol. 6, pp. 9375-9389, 2018.
- [8] Li X., Zhong A., Lin M., Guo N., Sitek A., Ye J., Thrall J., and Li Q., “Self-paced Convolutional Neural Network for Computer Aided Detection in Medical Imaging Analysis,” in *Proceedings International Workshop on Machine Learning in Medical Imaging*, Quebec, pp. 212-219, 2017.
- [9] Litjens G., Kooi T., Bejnordi B., Setio A., Ciompi F., Ghafoorian M., Laak J., Ginneken B., and Sánchez C., “A Survey on Deep Learning in Medical Image Analysis,” *Medical Image Analysis*, vol. 42, no. 9, pp. 60-88, 2017.
- [10] Ma L., Ma C., Liu Y., Wang X., and Xie W., “Diagnosis of Thyroid Diseases Using SPECT Mages Based On Convolutional Neural Network,” *Journal of Medical Imaging and Health Informatics*, vol. 8, no. 8, pp. 1684-1689, 2018.
- [11] Ma L., Ma C., Liu Y., and Wang X., “Thyroid Diagnosis from SPECT Images Using Convolutional Neural Network with Optimization,” *Computational Intelligence and Neuroscience*, pp. 1-11, 2019.
- [12] Martinez-Murcia F., Górriz J., Ramírez J., and Ortiz A., “Convolutional Neural Networks for Neuroimaging in Parkinson’s Disease: Is Preprocessing Needed?,” *International Journal of Neural Systems*, vol. 28, no. 10, pp. 1850035, 2018.
- [13] Martinez-Murcia F., Ortiz A., Górriz J., et al., “A 3D Convolutional Neural Network Approach for The Diagnosis of Parkinson’s Disease,” in *Proceedings International Work-Conference on the Interplay Between Natural and Artificial Computation*, Corunna, pp. 324-333, 2017.
- [14] Nair V., Hinton G., and Thorsten J., “Rectified linear Units Improve Restricted Boltzmann Machines,” in *Proceedings International Conference on Machine Learning*, Haifa, pp. 807-814, 2010.
- [15] Ortiz A., Munilla J., Martínez-Ibañez M., Górriz J., Ramírez J., and Salas-Gonzalez D., “Parkinson’s Disease Detection Using Isosurfaces-Based Features and Convolutional Neural Networks,” *Frontiers in Neuroinformatics*, vol. 13, pp. 48, 2019.
- [16] Ramakrishnan D. and Radhakrishnan K., “Applying Deep Convolutional Neural Network (DCNN) Algorithm in The Cloud Autonomous Vehicles Traffic,” *The International Arab Journal of Information Technology*, vol. 19, no. 2, pp. 186-194, 2022.
- [17] Ravi D., Wong C., Deligianni F., Berthelot M., Andreu-Perez J., Lo B., Yang G., “Deep learning for Health Informatics,” *IEEE Journal of Biomedical and Health Informatics*, vol. 21, no. 1, pp. 4-21, 2017.
- [18] Shen D., Wu G., and Suk H., “Deep Learning in Medical Image Analysis,” *Annual Review of Biomedical Engineering*, vol. 19, pp. 221-248, 2017.
- [19] Simonyan K. and Zisserman A., “Very Deep Convolutional Networks for Large-Scale Image Recognition,” arXiv 2014, arXiv:1409.1556, 2014.
- [20] Spier N., Christoph R., Rupperecht C., Navab N., Baust M., and Nekolla S., “Defect Detection in Cardiac SPECT Using Graph-Based Convolutional Neural Networks,” *Journal of*

Nuclear Medicine, vol. 59, no. 1, pp. 1541, 2018.

- [21] Tian J., Liu G., Gu S., JUZ., Liu J., and GU D., "Deep Learning in Medical Image Analysis and its Challenges," *Acta Automatica Sinica*, vol. 44, no. 3, pp. 401-424, 2018.



Qiang Lin received his Ph.D. in computer science and technology from Northwestern Polytechnical University, China in 2014. He is currently a Professor with the School of Mathematics and Computer Science, Northwest Minzu University. His research interest includes medical image computing, pervasive computing, intelligent information processing, and human behavior sensing.



Zhengxng Man received his M.S. in computer software and theory from Lanzhou University, China in 2005. He is currently a Professor with the School of Mathematics and Computer Science, Northwest Minzu University. His research interest includes medical image computing, software design, and intelligent information processing.



Yongchun Cao received his M.S. in computer application technology from University of Science and Technology of China, China in 2002. He is currently a Professor with the School of Mathematics and Computer Science, Northwest Minzu University. His research interest includes medical image computing, intelligent information processing, and human behavior sensing.



Haijun Wang received his chief physician in imaging and nuclear medicine in 2021. He is currently a director and Professor of Nuclear Medicine Department, Gansu Provincial Hospital. His research interest includes imaging diagnosis and radionuclide therapy.